



Analytical description of photonic waveguides with multilayer claddings: Towards on-chip generation of entangled photons and Bell states

Sergei V. Zhukovsky^{a,b,1}, Lukas G. Helt^a, Dongpeng Kang^b, Payam Abolghasem^b,
Amr S. Helmy^b, J.E. Sipe^{a,*}

^a Department of Physics and Institute for Optical Sciences, University of Toronto, 60 St. George Street, Toronto, Ontario, Canada M5S 1A7

^b The Edward S. Rogers Department of Electrical and Computer Engineering, University of Toronto, 10 King's College Road, Toronto, Ontario, Canada M5S 3G4



ARTICLE INFO

Article history:

Received 19 December 2012

Received in revised form

21 March 2013

Accepted 22 March 2013

Available online 17 April 2013

Keywords:

Bragg reflection waveguides (BRWs)

Spontaneous parametric downconversion
(SPDC)

Entangled photons

Quantum information

Second-order nonlinearities

ABSTRACT

We present a theoretical description of slab and ridge waveguides with multilayer claddings, such as Bragg reflection waveguides (BRWs), using analytical expressions based on Fresnel and Airy formulas. This approach simplifies the waveguide calculations in comparison with more traditional techniques such as the transfer matrix method or direct stitching of plane-wave solutions at layer interfaces. Approximate but simple and straightforward analytic relations describing the effective indices and group velocities of guided modes in arbitrary 1D BRWs are derived. The formalism is then extended to 2D ridge waveguides using the effective index method. The approach is employed to engineer BRWs where several types of phase matching are present simultaneously at the same wavelength, as well as BRWs where photons generated by spontaneous parametric downconversion have the maximal degree of polarization entanglement. These results promote the use of BRWs as on-chip entangled photon sources, and facilitate on-chip generation of multiple optical Bell states. The designs are based on the AlGaAs fabrication platform and are within reach of experimental realization.

© 2013 Elsevier B.V. All rights reserved.

1. Introduction

Waveguides carrying optical signals between functional elements of an integrated optical circuit are as basic to its functioning as conductive wires are to a microelectronic chip [1,2]. Moreover, waveguides form a basis for the design of functional elements themselves. This can be achieved either by altering the geometry of a waveguide, forming devices such as bottleneck-type [3] and microring-type resonators, add-drop filters, or directional couplers [4], or else by using the advanced functionality of the waveguide materials, such as nonlinear optical, electro-/magneto-optical, or gain effects. In particular, nonlinear optical waveguides can enable on-chip implementation of processes such as nonlinear frequency conversion, optical parametric oscillation, spontaneous four-wave mixing (SWFM), and spontaneous parametric downconversion (SPDC). The latter two are capable of producing entangled photons

and other nonclassical states of light, which is a primary objective in quantum optics [5,6].

To make full use of SPDC in integrated optical waveguides for the production of photons with a desired spectrum, polarization, and entanglement, there is a need to control both phase matching (PM) and mode dispersion. A highly promising approach is provided by making the waveguide support modes with two distinct guiding mechanisms, such as total internal reflection (TIR) for lower-frequency (downconverted) modes and Bragg reflection for higher-frequency (pump) modes [7]. Such structures, known as Bragg reflection waveguides [BRWs, see Fig. 1(a)], have been extensively investigated in the past five years. Both nonlinear frequency conversion [8–10] and SPDC [11–14] were theoretically predicted and experimentally demonstrated. It was shown that independent guiding mechanisms for TIR and Bragg modes make for a rich variety of possible PM types [13,15,16]. As a result, a single BRW-based source can generate differently polarized entangled photons, which is very promising because such a source has a potential of generating multiple orthogonal Bell states of two entangled photons [17]. These states form a complete basis and produce maximal violations of the Bell inequality, and are therefore widely used in quantum information science [18]. The complete set of Bell states can already be generated by a single SPDC process using post-chip compensation [18,19]. Still, an on-chip switchable source of multiple Bell states, integrated

* Corresponding author at: Department of Physics, Institute for Optical Sciences, University of Toronto, 60 St. George Street, Toronto, Ontario, Canada M5S 1A7. Tel.: +1 (416) 978-4517.

E-mail addresses: sezh@fotonik.dtu.dk (S.V. Zhukovsky), a.helmy@utoronto.ca (A.S. Helmy), sipe@physics.utoronto.ca (J.E. Sipe).

¹ Present address: DTU Fotonik, Department of Photonics Engineering, Technical University of Denmark, Ørsted Plads 343, DK-2800 Kgs. Lyngby, Denmark.

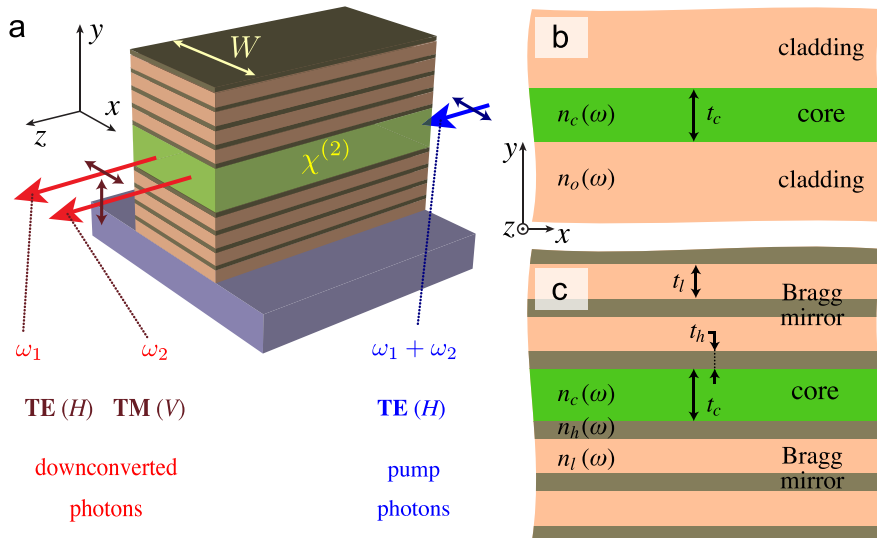


Fig. 1. Schematic of (a) a 2D ridge BRW (showing type-II SPDC). An enlarged view of a slab waveguide (b) without and (c) with refractive index modulation (Bragg mirror) in the cladding. Geometrical and material parameters used throughout the paper are shown.

with quantum-interference circuits [5,20,21], would bring many quantum optical experiments from an optical table to an optical chip, constituting a major breakthrough in photonic quantum technology [22].

The cladding of a BRW is essentially a periodic dielectric multilayer structure operating in the photonic band gap (PBG) regime, which provides total reflection only in the limit of an infinite number of periods. For actual claddings, a common way to minimize radiation losses is to design the cladding to operate exactly in the middle of the PBG by fulfilling the quarter-wave (QW) condition. Extensive theoretical investigations of such QW-BRWs have been performed [15,23,24]. It has been shown that significant mode dispersion control can be achieved by varying the core thickness [24] and ridge width [11].

However, while QW-BRWs represent an obvious starting point in a theoretical description of waveguides with multilayer claddings, they are certainly not the only possibility. It was shown recently that second-harmonic generation in BRWs can be dramatically increased by using a structured core rather than a single-layer core [10]. Additionally, varying the structured core composition can significantly alter the dispersion characteristics of all modes as well as the strength of the nonlinear mode interaction [25]. Furthermore, intentional departure from the QW condition can lead to simultaneous PM of more than one type; when used in SPDC, this leads to the generation of photon pairs entangled in a controllable number of degrees of freedom [26]. Finally, the PBG phenomenon is by no means unique to purely periodic systems, and it is highly likely that using a different cladding structure would change the characteristics of Bragg modes while having minimal influence over TIR modes.

Although the theory of multilayer structures is straightforward, and the set of modes supported by any multilayer-cladding waveguide can be easily determined with efficient numerical methods, the reverse problem, i.e., *designing* a waveguide to support a particular set of modes, is much more difficult and still largely open. The reason is that the equations describing even a simple slab dielectric waveguide are transcendental, and do not lend themselves to an exact analytical solution. The problem becomes increasingly more difficult when complex multilayer claddings are considered, and the design of structures that would suit a particular purpose is often a tedious process involving multiple-parameter optimization, sometimes even employing genetic algorithms [27].

It is therefore useful to develop analytical methods capable of predicting the behavior of multilayer waveguides, such as BRWs, prior to reverting to full numerical simulations and without having to make restrictive assumptions such as the QW condition. In this paper, we present such an analytical approach using a combination of Fresnel and recurrent Airy formulas applied to multilayer claddings of slab and ridge waveguides. We show that it is often possible to construct approximate but simple and straightforward analytical expressions describing the effective indices and group velocities of TIR and Bragg modes in arbitrary slab BRWs. In comparison to the more traditional transfer matrix methods or direct stitching of solutions of Maxwell's equation at layer interfaces [23,24], these expressions simplify the calculations involving multilayer waveguides, especially when inverse problems are involved. We also show that the effective index method can be readily used to extend the analytical formalism to 2D ridge waveguides for a wide range of waveguide parameters.

We demonstrate the approach by proposing several designs of BRWs where two or three distinct PM types are present simultaneously at the same pump wavelength, enriching the degree of polarization-driven control over nonlinear frequency conversion processes. We also propose several designs of BRWs for SPDC processes where the generated photon pairs have the maximal degree of polarization entanglement. Such BRW structures could serve as on-chip sources of entangled photons and optical Bell states. The results obtained are specifically tailored to the structures epitaxially grown on the AlGaAs platform, and are suitable for experimental realization.

The paper is organized as follows. In Section 2 the theoretical framework is presented. Slab dielectric waveguides, Bragg reflection waveguides, and 2D ridge waveguides with multilayer claddings are investigated. In Section 3, the approach is used to model several example devices suitable for simultaneous nonlinear frequency conversion and SPDC through multiple PM types. In Section 4 we combine our approach with a previously developed Hamiltonian formalism [28,29] to propose several model devices suitable for on-chip generation of co-polarized and cross-polarized polarization entangled photons, where the entanglement is not compromised by the difference in spectral properties of differently polarized downconverted photons. The improved quality of the polarization entanglement is numerically demonstrated in the calculation of the predicted results for standard quantum

interference experiments. Finally, in [Section 5](#) the main results of the paper are summarized.

2. Theoretical description

2.1. Fresnel and Airy formulas for multilayer structures

We first introduce the formalism and briefly review several background points that will be used throughout the paper. Consider a multilayer system which is homogeneous in the x and z directions but is piecewise homogeneous in the y direction [[Fig. 1\(b,c\)](#)]. Each constituent layer is a homogeneous medium where the solutions of Maxwell's equations can have plane-wave form

$$\mathbf{E}(\mathbf{r}, t) = \mathbf{E}_0 e^{i\mathbf{k}\cdot\mathbf{r}} e^{-i\omega t} + \text{c.c.} \quad (1)$$

In a homogeneous isotropic medium with refractive index n , the wave vector \mathbf{k} is related to the frequency ω through the dispersion relation,

$$\mathbf{k}^2 - (\omega/c)^2 n^2 = 0. \quad (2)$$

Since all layer interfaces are planes with y fixed, it is convenient to decompose [[Fig. 1\(b\)](#)]

$$\mathbf{k} = k_x \hat{\mathbf{x}} + k_z \hat{\mathbf{z}} + k_y \hat{\mathbf{y}} = \kappa \pm w \hat{\mathbf{y}}, \quad (3)$$

where k_x and k_z are taken to be real. Here κ is the component of the wave vector tangential to all layer interfaces; for any multilayer system, its value will be the same across all layers. For a wave that can propagate in some direction along the (x - z) plane, we call $\kappa = |\kappa|$ its propagation constant, and $n_{\text{eff}} = (c/\omega)\kappa$ is commonly defined as its effective index. The other, normal component of the wave vector $\pm w \hat{\mathbf{y}}$ has its magnitude w given by Eq. (2):

$$w = \sqrt{k^2 - \kappa^2} = (\omega/c) \sqrt{n^2 - n_{\text{eff}}^2}, \quad (4)$$

which, expectedly, is real only if $n_{\text{eff}} \leq n$, which is the existence condition of plane waves in a homogeneous medium. In general, the expression under the square root in Eq. (4) can be complex; the square root is chosen in such a way that $\text{Im } w \geq 0$, and if $\text{Im } w = 0$, then we take $\text{Re } w \geq 0$.

Now consider a plane interface between two such media [[Fig. 1\(b\)](#)] with refractive indices n_i and n_j . Writing the plane wave solutions in

the form (1) in each medium and using the boundary conditions at the interface to stitch these solutions together, the reflection and transmission coefficients of plane waves at the interface are found to be given by the well-known Fresnel formulas [30]

$$r_{ij}^{\text{TE}} = \frac{w_i - w_j}{w_i + w_j}, \quad r_{ij}^{\text{TM}} = \frac{w_i n_j^2 - w_j n_i^2}{w_i n_j^2 + w_j n_i^2}, \quad (5)$$

$$t_{ij}^{\text{TE}} = \frac{2w_i}{w_i + w_j}, \quad t_{ij}^{\text{TM}} = \frac{2w_i n_i n_j}{w_i n_j^2 + w_j n_i^2}, \quad (6)$$

where

$$w_{i,j} = (\omega/c) \sqrt{n_{i,j}^2 - n_{\text{eff}}^2}. \quad (7)$$

The coefficients r_{ij} and t_{ij} are dependent on whether the field is TE- (s -) polarized or TM- (p -) polarized; these polarization states can be considered separately in plane-parallel geometries [31]. For $n_j < n_{\text{eff}} < n_i$, w_i is real and w_j is purely imaginary, resulting in $|r_{ij}| = 1$ and signifying the case of total internal reflection, with the wave evanescent in the medium j .

Finally, consider one layer of refractive index n_c and thickness t_c , sandwiched between media with refractive indices n_i and n_j . We can write the reflection and transmission coefficients of such a structure in the form of Airy formulas

$$R_{ij}^{(c)} = r_{ic} + \frac{t_{ic} r_{cj} t_{cj} e^{2iw_c t_c}}{1 - r_{ci} r_{cj} e^{2iw_c t_c}} = \frac{r_{ci}(-1 + e^{2iw_c t_c})}{1 - r_{ci} r_{cj} e^{2iw_c t_c}}, \quad (8)$$

$$T_{ij}^{(c)} = \frac{t_{ic} t_{cj} e^{iw_c t_c}}{1 - r_{ci} r_{cj} e^{2iw_c t_c}}. \quad (9)$$

Like the Fresnel interface coefficients of Eqs. (5) and (6), $R_{ij}^{(c)}$ and $T_{ij}^{(c)}$ are different for TE- and TM-polarized waves.

2.2. Simple slab waveguides: mode effective indices

The dielectric multilayer systems we consider will support a guided mode with the effective index n_{eff} if in some layers it has a real-valued w whereas in the surrounding layers w is imaginary, confining the wave in the y -direction. The simplest system of that kind is a symmetric slab waveguide where the core layer has refractive index n_c and thickness t_c , surrounded by an outer

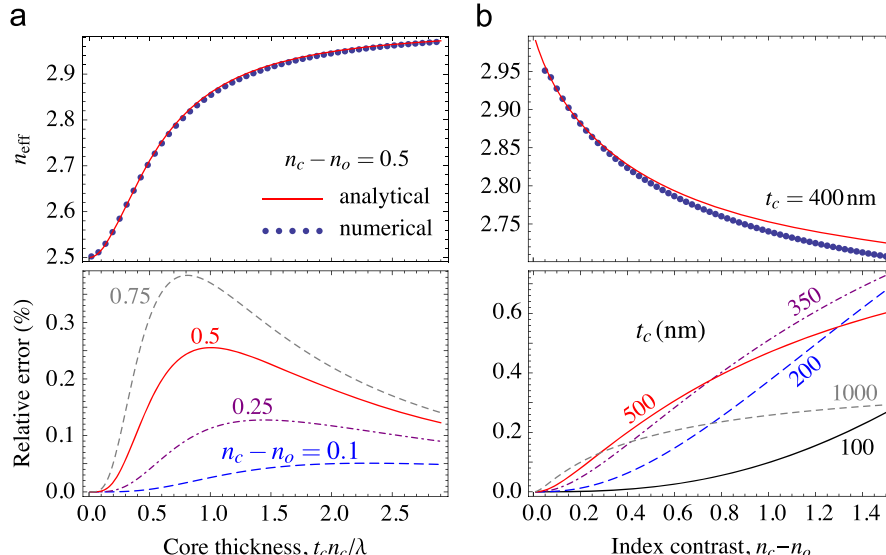


Fig. 2. Comparison between fundamental-mode effective index $n_{\text{eff}}^{\text{TE}}$ obtained by numerically solving Eq. (10) and analytically from Eq. (16) for a slab waveguide: (a) with varying core thickness and (b) with varying core/cladding refractive index contrast for $\lambda = 1550$ nm and $n_c = 3.0$; the remaining parameters are as marked. Bottom plots show the relative error between analytical and numerical calculations.

cladding with index $n_o < n_c$ [Fig. 1(b)]. Modes can be guided in the core due to the total internal reflection (TIR) if $n_o < n_{\text{eff}} < n_c$.

The standard approach to determine the values of n_{eff} for which waveguiding is possible consists in using the boundary conditions at layer interfaces to stitch together the plane-wave solution of Maxwell's equations in each layer, and then solving the eigenvalue equation for n_{eff} [32]. An alternative approach is to look for conditions when the reflection and transmission coefficients in Eqs. (8) and (9) diverge, indicating the presence of reflected and transmitted fields in the absence of an incident wave [33]. This can be obtained if there is a pole in Eqs. (8) and (9) [34,35], i.e.,

$$1 - r_{co}^2 \exp(2iw_ct_c) = 0, \quad (10)$$

where r_{co} for each polarization is given by Eqs. (5) and (6) and $w_{c,o}$ are determined from Eq. (7). If $n_o < n_{\text{eff}} < n_c$, we see that $w_c \equiv h_c \omega/c$ is real while $w_o \equiv ih_o \omega/c$ is imaginary, so $|r_{co}| = 1$ as expected for TIR modes. The quantities h_c and h_o are introduced for brevity of notation and equal

$$h_c = \sqrt{n_c^2 - n_{\text{eff}}^2}, \quad h_o = \sqrt{n_{\text{eff}}^2 - n_o^2}. \quad (11)$$

Since $|r_{co}| = 1$, putting $r_{co} = \exp(i\delta_r)$ we can rewrite Eq. (10) as

$$\exp[i(2\delta_r + 2w_ct_c)] = 1, \quad (12)$$

from where, after some algebra [36], it follows that the effective indices of TE-polarized guided modes are determined by a set of transcendental equations

$$\frac{\cos x}{x} = \pm \frac{1}{V}, \quad \frac{\sin x}{x} = \pm \frac{1}{V}, \quad (13)$$

where $x = w_ct_c/2$, and

$$V = \frac{\omega t_c}{c} \sqrt{n_c^2 - n_o^2} \quad (14)$$

can be viewed as the “strength of the waveguide potential” [36].

For the fundamental mode, which corresponds to the smallest root of the cosine equation in (13), we can Taylor expand the cosine for small x , yielding:

$$\frac{\cos x}{x} = \frac{1}{x} - \frac{x}{2} + O(x^3), \quad (15)$$

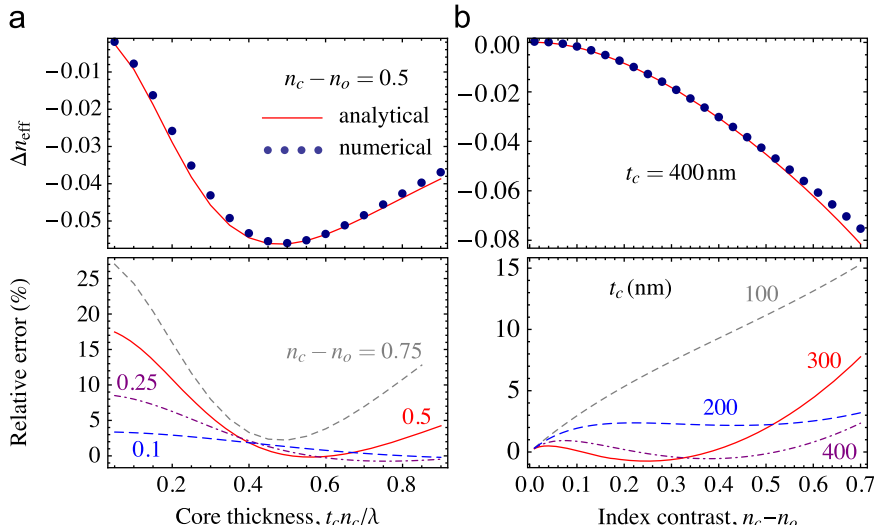


Fig. 3. Comparison between Δn_{eff} obtained by numerically solving Eq. (10) and analytically from Eq. (19) for a slab waveguide: (a) with varying core thickness and (b) with varying core/cladding refractive index contrast for $\lambda = 1550$ nm and $n_c = 3.0$; the remaining parameters are as marked. Bottom plots show the relative error between analytical and numerical calculations.

which results in an approximate analytic expression for the fundamental-mode $n_{\text{eff}}^{\text{TE}}$:

$$n_{\text{eff}}^{\text{TE}} \approx \sqrt{n_c^2 - \left[\frac{(\sqrt{2} V^2 + 1 - 1)/V}{\omega t_c/(2c)} \right]^2}. \quad (16)$$

Fig. 2 compares this analytic expression with the numeric result of solving Eq. (13) for a slab waveguide with the core refractive index $n_c = 3.0$ and varying core thickness and cladding refractive index. We see that Eq. (16) correctly reproduces the effective index of the fundamental TE mode to within 1% accuracy over a wide range of waveguide parameters.

To determine the index splitting Δn_{eff} between the TE- and TM-polarized modes, we rewrite Eqs. (5) in the form

$$\delta_r^{\text{TE}} = \arctan \frac{-2h_c h_o}{n_c^2 + n_o^2 - 2n_{\text{eff}}^2}, \quad (17)$$

$$\delta_r^{\text{TM}} = \arctan \frac{-2h_c h_o}{n_c^2 + n_o^2 - \frac{n_c^4 + n_o^4}{n_c^2 n_o^2} n_{\text{eff}}^2}. \quad (18)$$

Since $(n_c^4 + n_o^4)/(n_c^2 n_o^2) \gtrsim 2$, we can Taylor expand δ_r to obtain the approximate value of

$$\Delta n_{\text{eff}} = n_{\text{eff}}^{\text{TM}} - n_{\text{eff}}^{\text{TE}} \approx \frac{\frac{2(n_{\text{eff}}^{\text{TE}})^2}{n_o^2 n_c^2} h_c^{\text{TE}} h_o^{\text{TE}}}{\frac{\partial \delta_r^{\text{TE}}}{\partial n_{\text{eff}}} - \frac{\omega}{c} \frac{n_{\text{eff}}^{\text{TE}} t_c}{h_c^{\text{TE}}}}. \quad (19)$$

The effective index $n_{\text{eff}}^{\text{TE}}$ of a TE-polarized mode can be obtained either numerically by solving Eq. (10) or, for the case of fundamental mode, analytically from Eq. (16). Once $n_{\text{eff}}^{\text{TE}}$ is found, Eq. (19) can be used to obtain the effective index $n_{\text{eff}}^{\text{TM}}$ of a corresponding TM-polarized mode. Fig. 3 demonstrates that Eq. (19) is accurate to within 5–10% for typical slab waveguides with index contrast $n_c - n_o$ not exceeding 0.5 and core thickness over 100 nm.

2.3. Simple slab waveguides: group velocities

The group velocity of a guided mode

$$v_g = c \left[n_{\text{eff}} + \omega \frac{dn_{\text{eff}}}{d\omega} \right]^{-1}, \quad (20)$$

can be expressed analytically in terms of n_{eff} . Taking the derivatives of the left-hand side of Eq. (10) with respect to ω and n_{eff} , we have

$$\frac{dn_{\text{eff}}}{d\omega} = -\frac{\frac{\partial \delta_r}{\partial \omega} + \frac{t_c}{c} h_c + \frac{\omega}{c} \frac{n_c t_c}{h_c} \frac{\partial n_c}{\partial \omega}}{\frac{\partial \delta_r}{\partial n_{\text{eff}}} - \frac{\omega}{c} \frac{n_{\text{eff}} t_c}{h_c}}. \quad (21)$$

The derivatives of δ_r with respect to frequency are determined by material dispersion:

$$\frac{\partial \delta_r^{\text{TE}}}{\partial \omega} = 2 \frac{\frac{h_o}{h_c} n_c \frac{\partial n_c}{\partial \omega} + \frac{h_c}{h_o} n_o \frac{\partial n_o}{\partial \omega}}{n_c^2 - n_o^2}, \quad (22)$$

$$\frac{\partial \delta_r^{\text{TM}}}{\partial \omega} = 2 \frac{\left(\frac{h_o}{h_c} n_c \frac{\partial n_c}{\partial \omega} + \frac{h_c}{h_o} n_o \frac{\partial n_o}{\partial \omega} \right) + \Delta}{(n_c^2 - n_o^2)[1 + \eta]}, \quad (23)$$

while the derivatives of δ_r with respect to n_{eff} are non-zero even for dispersionless media:

$$\frac{\partial \delta_r^{\text{TE}}}{\partial n_{\text{eff}}} = -2 \frac{n_{\text{eff}} \left(\frac{h_o}{h_c} + \frac{h_c}{h_o} \right)}{n_c^2 - n_o^2}, \quad (24)$$

$$\frac{\partial \delta_r^{\text{TM}}}{\partial n_{\text{eff}}} = -2 \frac{n_{\text{eff}} \left(\frac{h_o}{h_c} + \frac{h_c}{h_o} \right)}{(n_c^2 - n_o^2)[1 + \eta]}, \quad (25)$$

where the correction terms in Eqs. (23) and (25) are

$$\Delta = 2h_c h_o \left(\frac{1}{n_o} \frac{\partial n_o}{\partial \omega} - \frac{1}{n_c} \frac{\partial n_c}{\partial \omega} \right), \quad (26)$$

$$\eta = \frac{n_{\text{eff}}^2 - n_o^2}{n_o^2} + \frac{n_{\text{eff}}^2 - n_c^2}{n_c^2}. \quad (27)$$

Making use of $\Delta n_{\text{eff}} \ll n_{\text{eff}}$, we can determine the difference between group velocities $\Delta v_g = v_g^{\text{TM}} - v_g^{\text{TE}}$ by taking the Taylor expansion of Eq. (20) with respect to Δn_{eff} , Δ , and η . The final

expression reads

$$\begin{aligned} \Delta v_g(n_{\text{eff}}) \approx & -\frac{c}{\left(n_{\text{eff}} + \omega \frac{dn_{\text{eff}}}{d\omega} \right)^2} \left[\left(1 + \omega \frac{\partial}{\partial \omega} \frac{dn_{\text{eff}}}{d\omega} \right) \Delta n_{\text{eff}} \right. \\ & - \frac{\omega}{\partial \delta_r} - \frac{\omega}{c} \frac{n_{\text{eff}} t_c}{h_c} \left(-\frac{\partial \delta_r}{\partial \omega} \eta_m + \frac{2\Delta}{n_c^2 - n_o^2} \right) \\ & \left. - \omega \frac{\partial \delta_r}{\partial \omega} + \frac{t_c}{c} h_c + \frac{\omega}{c} \frac{n_c t_c}{h_c} \frac{\partial n_c}{\partial \omega} \frac{\partial \delta_r}{\partial n_{\text{eff}}} \right] \\ & \left. - \frac{\left(\frac{\partial \delta_r}{\partial n_{\text{eff}}} - \frac{\omega}{c} \frac{n_{\text{eff}} t_c}{h_c} \right)^2}{\left(\frac{\partial \delta_r}{\partial n_{\text{eff}}} - \frac{\omega}{c} \frac{n_{\text{eff}} t_c}{h_c} \right)^2} \eta \right]. \end{aligned} \quad (28)$$

Within these approximations, we only require $n_{\text{eff}} = n_{\text{eff}}^{\text{TE}}$ as the input parameter, to be found by solving a transcendental equation or, for the case of fundamental modes, analytically from Eq. (16). Fig. 4 compares Eq. (28) with numerically obtained Δv_g in $\text{Al}_x\text{Ga}_{1-x}\text{As}$ slab waveguides, where the refractive index $n(x, \omega)$ depends both on the frequency ω and on the Al concentration x [37]. We see that Eq. (28) predicts the correct Δv_g with absolute error not exceeding 0.02 $\mu\text{m}/\text{ps}$, unless both the core/cladding index contrast is extreme ($x_0 - x_c > 0.4$) and the core thickness is in the range $0.4 < t_c n_c / \lambda < 0.8$. While the presence of material dispersion modifies the group velocities quite significantly, it has almost no effect on the accuracy of Eq. (28).

2.4. Bragg reflection waveguides

Now consider a slab waveguide with multilayer claddings where the claddings are semi-infinite periodic structures made of alternating high-index and low-index layers (one-dimensional Bragg mirrors). These layers have refractive indices n_h, n_l and thicknesses t_h, t_l , respectively [Fig. 1(c)]. The reflection coefficient from such a cladding R_∞ , which for this new structure should replace r_{co} in Eq. (10), can be analytically determined using Airy formulas similar to Eqs. (8) and (9). With $R_{cc}^{(h)}, R_{cc}^{(l)}$ given by Eq. (8) and $T_{cc}^{(h)}, T_{cc}^{(l)}$ given by Eq. (9) with the subscripts $i, j = c$, and inserting an imaginary layer with zero thickness between the high- and low-index layers, we can use Eqs. (8) and (9) again to arrive at the reflection and transmission

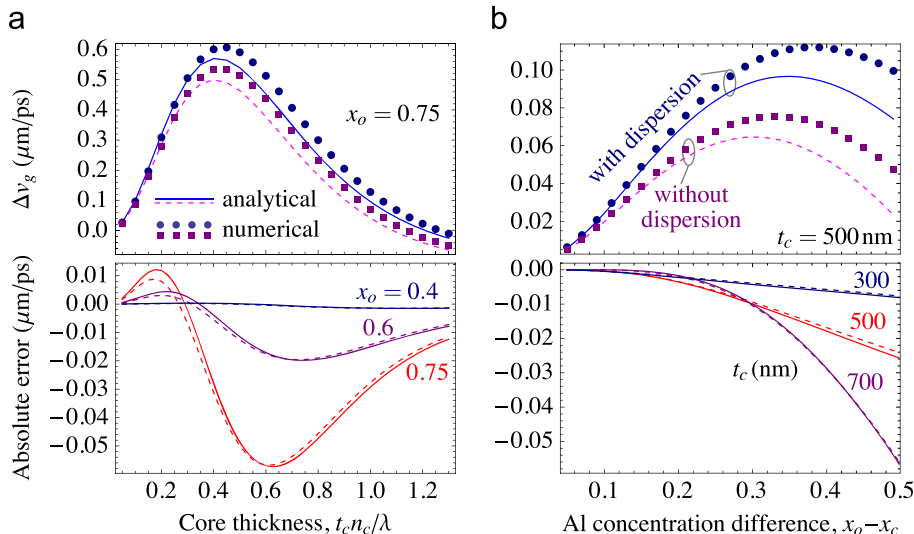


Fig. 4. Comparison between Δv_g obtained by numerically solving Eqs. (10) and (20) vs. analytically from Eq. (28) for a slab waveguide made of $\text{Al}_x\text{Ga}_{1-x}\text{As}$: (a) with varying core thickness and (b) with varying Al concentration between core and cladding for $\lambda = 1550 \text{ nm}$ and $x_c = 0.25$ ($n_c \approx 3.0$ at room temperature); the remaining parameters are as marked. Solid lines and circles, full calculation; dashed lines and squares, calculation with neglected material dispersion in $\text{Al}_x\text{Ga}_{1-x}\text{As}$. Bottom plots show the absolute error (in $\mu\text{m}/\text{ps}$) between analytical and numerical calculations.

coefficients for a bilayer [38]:

$$R_{cc}^{(hl)} = R_{cc}^{(h)} + \frac{[T_{cc}^{(h)}]^2 R_{cc}^{(l)}}{1 - R_{cc}^{(h)} R_{cc}^{(l)}}, \quad R_{cc}^{(lh)} = R_{cc}^{(l)} + \frac{[T_{cc}^{(l)}]^2 R_{cc}^{(h)}}{1 - R_{cc}^{(h)} R_{cc}^{(l)}}, \quad (29)$$

$$T_{cc}^{(hl)} = T_{cc}^{(lh)} = \frac{T_{cc}^{(h)} T_{cc}^{(l)}}{1 - R_{cc}^{(h)} R_{cc}^{(l)}}. \quad (30)$$

A semi-infinite periodic cladding remains unchanged if one of its periods is stripped away [see Fig. 5(a)]. Hence, these coefficients are related to R_∞ as [see Eq. (8)]

$$R_\infty = R_{cc}^{(hl)} + \frac{T_{cc}^{(hl)} R_\infty T_{cc}^{(lh)}}{1 - R_\infty R_{cc}^{(hl)}}. \quad (31)$$

This is a quadratic equation for R_∞ with two solutions. Only one of them, which corresponds to a decaying (rather than growing) field inside the multilayer, should be chosen as the physically correct value of R_∞ .

For QW BRWs,

$$w_h t_h = w_l t_l = \pi/2, \quad (32)$$

so $R_\infty^2 = 1$, and the pole condition in the form of Eq. (10) can be solved easily. The relevant analysis can be found in earlier work

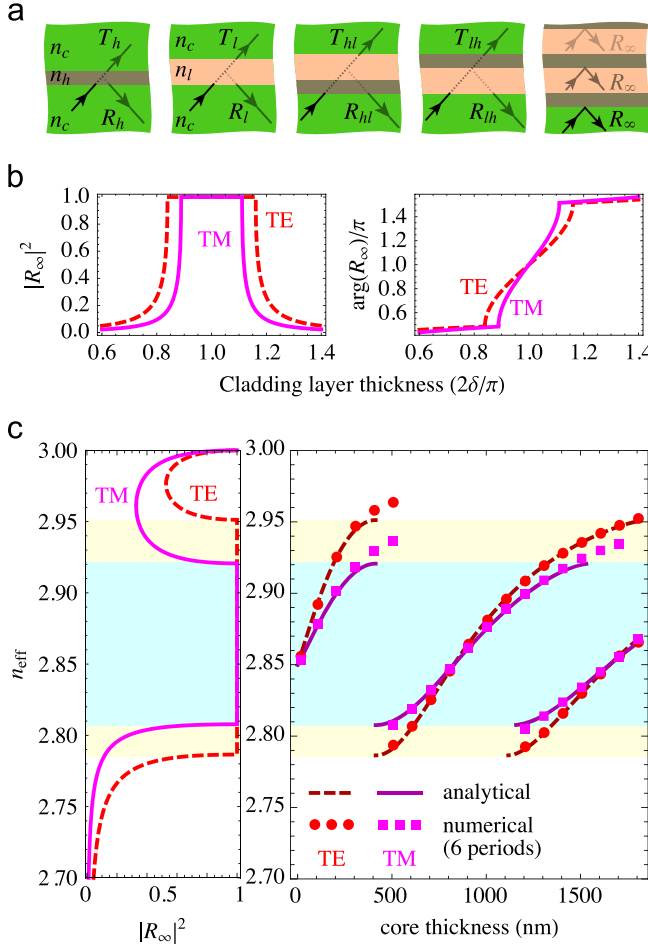


Fig. 5. (a) Illustration to the derivation of the Bragg cladding reflection coefficient R_∞ in Eqs. (29)–(31), (b) intensity and phase of R_∞ obtained from Eq. (31) for different $\delta = w_h t_h = w_l t_l$. The structure is a BRW with $n_h = 3.25$ and $n_l = n_c = 3.0$, which satisfies the QW condition ($\delta = \pi/2$) for 1550 nm and $n_{\text{eff}} = 2.85$ at $t_h = 248.1$ nm, $t_l = 413.7$ nm, (c) the dependence $|R_\infty(n_{\text{eff}})|^2$ for the same QW Bragg cladding, showing a photonic band gap around $n_{\text{eff}} = 2.85$ (shaded regions), along with mode diagrams for a BRW with varying core thickness t_c . Analytical results for infinite-period claddings (lines), obtained by solving Eq. (10) with r_{co} replaced by R_∞ , are compared with the results of direct 1D numerical simulations [39] for 6-period claddings (shown as dots).

[15,23,24]. In a more general case, the expression for the cladding reflection coefficient R_∞ , albeit rather bulky, can still be obtained analytically. We plot the amplitude and phase of R_∞ in Fig. 5(b) as a function of $\delta = w_h t_h = w_l t_l$. As expected, the cladding can function in two regimes: the pass band where $|R_\infty|^2 < 1$ and no guided modes can be supported, and the stop band or band gap around $\delta = \pi/2$, where $|R_\infty|^2 = 1$ and the Bragg reflection in infinite-period claddings effectively functions like total internal reflection for the waves in the core, resulting in guided modes. The phase $\arg(R_\infty)$ varies monotonically around π throughout the band gap.

Note that R_∞ becomes polarization dependent everywhere outside the QW point [24], reflecting the different widths of the band gap for TE- vs. TM-polarized modes. Hence, $\arg(R_\infty^{\text{TE}}) \neq \arg(R_\infty^{\text{TM}})$ whenever the frequency is off the middle point of the PBG, as defined by the QW condition. According to Eq. (10), this phase mismatch results in $n_{\text{eff}}^{\text{TE}} \neq n_{\text{eff}}^{\text{TM}}$. Indeed, Fig. 5(c) illustrates this by showing the mode structure of a BRW with varying core thickness t_c .

In Fig. 5(c) we also compare the mode effective indices predicted using the infinite-period cladding reflection coefficients, R_∞ [see Eq. (31)], in place of r_{co} in Eq. (10) with numerical results. The numerical results were obtained from a fully vectorial mode solver (Lumerical MODE SOLUTIONS [39]) that treated the BRW as having a finite number of periods N in the claddings. Even with N as low as 6, good agreement can be seen everywhere except in the immediate vicinity of the band edges where the reflectivity of finite-period Bragg mirrors is expectedly poor. This poor reflectivity causes the edges of a photonic band gap to smear, causing discrepancies between the analytical and numerical results, as well as the existence of extremely lossy guided modes slightly beyond the band edges of an infinite-period cladding.

2.5. Two-dimensional ridge waveguides

For realistic applications of waveguides where light is guided along one direction and confined in the remaining dimensions, a slab multilayer structure is usually etched to form a ridge or strip-loaded waveguide [Fig. 1(a)]. Determining the effective index in these waveguides normally requires solving the wave equations in 2D. Rigorous analytical solutions are only available for simple geometries. Still, if the ridge is sufficiently wide compared to the core thickness, the effective-index method can be employed [31] to apply the 1D results described above to ridge waveguides while keeping the relevant expressions simple and analytic.

Consider that a slab waveguide of arbitrary geometry is made into a ridge of width $W \gg t_c$, suppose that the effective indices for the slab waveguide are denoted $n_{1D}^{\text{TE,TM}}$, and that the ridge is surrounded by an ambient medium with refractive index n_a . The effective medium method dictates that the ridge waveguide modes should be found by analyzing the pole condition for the direction perpendicular to the channel [x in Fig. 1(a)], assuming the core to be made of material with $n = n_{1D}^{\text{TE,TM}}$, i.e.,

$$1 = (\tilde{r}_{ca}^{\text{TE,TM}})^2 \exp \left[2i \frac{\omega}{c} W \sqrt{(n_{1D}^{\text{TE,TM}})^2 - (n_{2D}^{\text{TE,TM}})^2} \right], \quad (33)$$

where

$$\tilde{r}_{ca}^{\text{TE}} = \frac{n_a^2 \sqrt{(n_{1D}^{\text{TE}})^2 - (n_{2D}^{\text{TE}})^2} - i(n_{1D}^{\text{TE}})^2 \sqrt{(n_{2D}^{\text{TE}})^2 - n_a^2}}{n_a^2 \sqrt{(n_{1D}^{\text{TE}})^2 - (n_{2D}^{\text{TE}})^2} + i(n_{1D}^{\text{TE}})^2 \sqrt{(n_{2D}^{\text{TE}})^2 - n_a^2}}, \quad (34)$$

and

$$\tilde{r}_{ca}^{\text{TM}} = \frac{\sqrt{(n_{1D}^{\text{TM}})^2 - (n_{2D}^{\text{TM}})^2} - i\sqrt{(n_{2D}^{\text{TM}})^2 - n_a^2}}{\sqrt{(n_{1D}^{\text{TM}})^2 - (n_{2D}^{\text{TM}})^2} + i\sqrt{(n_{2D}^{\text{TM}})^2 - n_a^2}}. \quad (35)$$

We note that these are essentially Fresnel's formulas [cf. Eq. (5)] between the material with refractive index equal to the 1D effective index, and the ambient medium, and that TE and TM-polarization expressions are reversed because a mode that is TE-polarized with respect to the layer interfaces [$x-z$ planes in Fig. 1(a)] is TM-polarized with respect to the ridge sides [$y-z$ planes in Fig. 1(a)], and vice versa [31].

Since $|\tilde{r}_{ca}^{TE,TM}| = 1$, Eq. (33) reduces to

$$\arg \tilde{r}_{ca}^{TE,TM} + \frac{\omega}{c} W \sqrt{(n_{1D}^{TE,TM})^2 - (n_{2D}^{TE,TM})^2} = \pi m, \quad (36)$$

where the integer $m = 1, 2, \dots$ numbers the modes with different order with respect to the number of maxima in the direction of the ridge. Physically, m is the number of half-waves accommodated within a ridge with a width W .

The condition $W \gg t_c$ assures that the effective indices of the 2D modes do not deviate very much from those of the 1D modes, especially for lower m . Hence, as a first-order approximation, we can assume that $n_{2D}^{TE,TM} \approx n_{1D}^{TE,TM}$ everywhere except where these two quantities are subtracted, i.e., we assume that in Eqs. (34) and (35)

$$\sqrt{(n_{2D}^{TE,TM})^2 - n_a^2} \approx \sqrt{(n_{1D}^{TE,TM})^2 - n_a^2}. \quad (37)$$

We can then Taylor expand the remaining function using $n_{1D}^2 - n_{2D}^2$ as the small parameter. As a result, Eq. (36) can be further transformed and solved for the effective index $n_{2D}^{TE,TM}$ for the mode of the order m as

$$(n_{2D,m}^{TE})^2 = (n_{1D}^{TE})^2 - \frac{(m\pi)^2}{\left[\frac{\omega}{c} W + \frac{2n_a^2/(n_{1D}^{TE})^2}{\sqrt{(n_{1D}^{TE})^2 - n_a^2}} \right]^2} \quad (38)$$

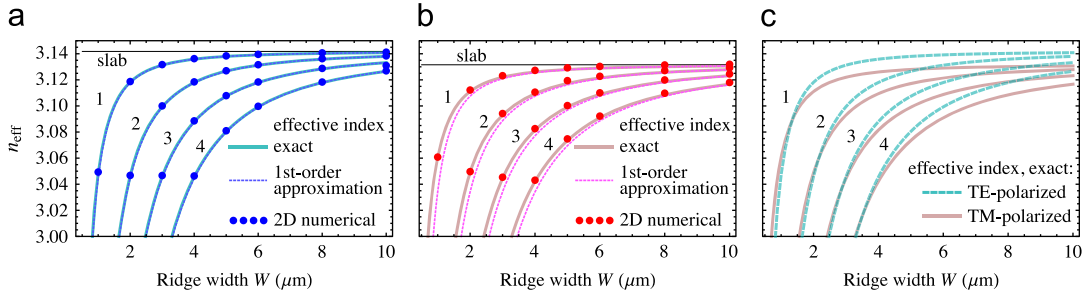


Fig. 6. Dependence of n_{eff} on the ridge width W of a 2D ridge waveguide obtained by the effective index method, based on numerical solution of the exact pole condition (33) ("exact", solid lines) and calculated from the first-order approximation Eqs. (38) and (39) ("1st-order", dotted lines) for the first four orders of (a) TE- and (b) TM-polarized modes; (c) shows both polarizations in overlay. For the TE case, the solid and dotted lines are almost indistinguishable. The results obtained from a fully vectorial eigenmode solver [39] are shown as dots. The structure parameters are $n_c = 3.25$, $t_c = 500$ nm, $n_o = 3.0$ for $\lambda = 1550$ nm.

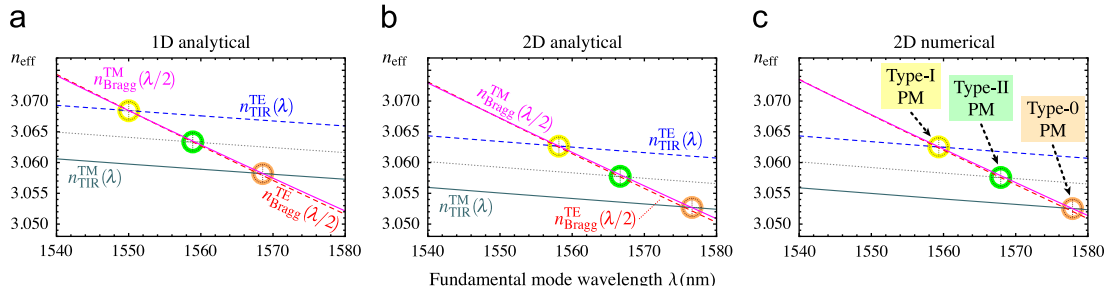


Fig. 7. Dispersion curves for TIR-guided fundamental (downconverted) and Bragg-guided SH (pump) modes of a BRW showing type-I, type-II, and type-0 PM: (a) 1D analytical results for a slab waveguide with an infinite number of periods in the claddings, (b) 2D analytical results for a ridge waveguide with $W = 4.4 \mu\text{m}$ and an infinite number of periods, given by the effective index method and (c) 2D numerical results for a ridge waveguide with 6 periods in the claddings, obtained by a fully vectorial eigenmode solver [39]. The parameters are $x_c = 0.62$, $t_c = 392$ nm; $x_h = 0.2$, $t_h = 111$ nm; $x_l = 0.8$, $t_l = 341$ nm. Here and further, the gray dotted line shows $(n_{\text{TIR}}^{\text{TE}} + n_{\text{TIR}}^{\text{TM}})/2$.

and

$$(n_{2D,m}^{\text{TM}})^2 = (n_{1D}^{\text{TM}})^2 - \frac{(m\pi)^2}{\left[\frac{\omega}{c} W + \frac{2}{\sqrt{(n_{1D}^{\text{TM}})^2 - n_a^2}} \right]^2}. \quad (39)$$

Fig. 6 shows the comparison of these first-approximation equations with the exact result obtained numerically from the pole condition (33), as well as with the results of direct 2D numerical simulations. We note that the results of the exact and the approximate effective-index method nearly coincide, and show an excellent agreement with the eigenmode solver simulations down to very narrow ($1 \mu\text{m}$) ridges, as long as $n_{2D,m}^{\text{TE,TM}} > n_o$ so that guiding in the y -direction still persists.

Note that in the strip-loaded configuration, the results are just as applicable if the effective index $n_{1D,\text{out}}$ in the regions outside the strip is calculated and used in place of n_a . Obviously, since $n_{1D,\text{out}} \lesssim n_{1D}$, the number of modes will be limited by the applicable range of effective indices for $n_{2D,m}$ defined by $n_{1D,\text{out}} < n_{2D,m} < n_{1D}$.

3. Multiple-type phase matching

As we have seen in the previous section, many properties of waveguides with multilayer claddings can be intuitively understood from simple analytical expressions involving the Airy formulas for the Fresnel reflection coefficients of the claddings. For example, we see that form birefringence for the index-guided modes in a slab waveguide is primarily determined by the ridge width (Fig. 6, see [40,41]) while form birefringence for the Bragg-guided modes is strongly influenced by the QW condition in the claddings (Fig. 5, see [24]).

This knowledge is especially valuable in a device where index-guided modes at a certain frequency ω and Bragg-guided modes at second-harmonic frequency 2ω are phase matched for on-chip SHG or SPDC [15]. Fig. 7 shows such PM in a typical QW-BRW. We see that PM of multiple types is present, including standard type-I ($\text{TM}_{2\omega} \leftrightarrow \text{TE}_\omega + \text{TE}_\omega$) and type-II ($\text{TE}_{2\omega} \leftrightarrow \text{TE}_\omega + \text{TM}_\omega$), as well as type-0 [42,43] ($\text{TM}_{2\omega} \leftrightarrow \text{TM}_\omega + \text{TM}_\omega$, also referred to as type-IV). Still, these processes are several nanometers apart from each other due to form birefringence in the index-guided modes [see Eq. (19)]. In what follows, we show how the design principles outlined above can be used to realize more than one PM type at the same wavelength. Such simultaneous multiple-type PM can be beneficial for high-power continuous-wave SHG [44,45]. It is also useful in SPDC because the entanglement characteristics of the generated photon pairs depend on the PM type, and can be switched simply by rotating the polarization of the pump beam [26].

3.1. Simultaneous phase matching of two types

For simultaneous type-I and type-II PM at a frequency ω_0 , we require

$$\begin{aligned} n_{\text{eff}}^{\text{TM}}(2\omega_0) &= n_{\text{eff}}^{\text{TE}}(\omega_0), \\ n_{\text{eff}}^{\text{TE}}(2\omega_0) &= (n_{\text{eff}}^{\text{TE}}(\omega_0) + n_{\text{eff}}^{\text{TM}}(\omega_0))/2, \end{aligned} \quad (40)$$

and for simultaneous type-0 and type-II PM, we require

$$\begin{aligned} n_{\text{eff}}^{\text{TM}}(2\omega_0) &= n_{\text{eff}}^{\text{TM}}(\omega_0), \\ n_{\text{eff}}^{\text{TE}}(2\omega_0) &= (n_{\text{eff}}^{\text{TE}}(\omega_0) + n_{\text{eff}}^{\text{TM}}(\omega_0))/2. \end{aligned} \quad (41)$$

To bring two PM types to the same wavelength, form birefringence in the index-guided modes should be compensated by form birefringence in the Bragg modes, so that $\Delta n(2\omega_0) = \pm \Delta n(\omega_0)/2$. This can already be done in a 1D slab geometry, by veering the waveguide geometrical parameters off the QW condition. Indeed, any perturbation of the QW condition (a change in $\delta_i = w_i t_i$ where i stands for c , l , or h) will create a controllable shift between n_{eff} for the TE vs. TM-polarized Bragg modes. Changing the thicknesses of the core and/or cladding layers $t_{c,l,h}$ is a more preferable way to alter $\delta_{c,l,h}$ than changing the refractive indices $n_{c,l,h}$ because the latter exerts more influence over the index-guided modes. Fig. 8(a) shows how $n_{\text{TE}} - n_{\text{TM}}$ for Bragg-guided modes can be controlled by varying the layer thicknesses.

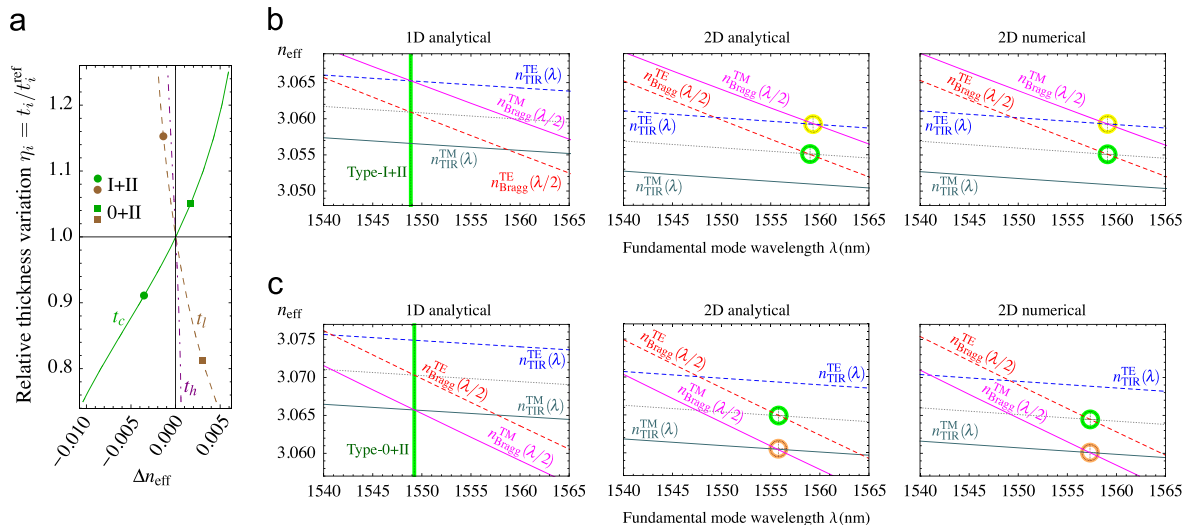


Fig. 8. (a) The dependence of $\Delta n_{\text{eff}} = n_{\text{eff}}^{\text{TM}} - n_{\text{eff}}^{\text{TE}}$ for the Bragg modes on the variation of layer thicknesses $t_{c,l,h}$ with respect to the reference structure in Fig. 7. Dispersion relations of (b) structure with simultaneous type-I and type-II PM; (c) structure with simultaneous type-II and type-0 PM. Left: Analytical results for a 1D slab waveguide with semi-infinite claddings, obtained from Eq. (31). Middle: Analytical results for a 2D ridge waveguide. Right: Numerical results from fully vectorial 2D simulation [39]. The operating points for (b) and (c) are denoted in the plots (a) as circles and squares, respectively.

To keep the PM wavelength near 1550 nm and to further enhance the difference between n_{TE} and n_{TM} , both t_c and t_l should be varied with opposite signs. A structure with t_c decreased by 33.2 nm and t_l increased by 50 nm (compared to the QW structure in Fig. 7) has $\Delta n = -0.0045$, which results in simultaneous PM for type-I and type-II SPDC. A structure with t_c increased by 18.5 nm and t_l decreased by 64 nm has $\Delta n = +0.0045$, resulting in simultaneous PM for type-II and type-0 SPDC.

These examples are presented in Fig. 8, indeed showing simultaneous type-I+type-II [Fig. 8(b)] and type-II+type-0 [Fig. 8(c)] PM in SPDC. We have also verified our 1D results for a moderate-width (4.4 μm) ridge waveguide using both analytical calculations and numerical simulations. The property of simultaneous multiple-type PM is seen to persist in the 2D case with good accuracy, despite the systematic shifts in the effective index and PM wavelengths, and deviations between the analytical and numerical results are minimal. For 8-period claddings, non-QW BRWs have increased radiation losses in the Bragg modes by several times compared to the reference QW-BRWs. Still, the losses do not exceed 0.2 dB/cm, which is acceptable in waveguides several millimeters long.

When pumped by TE-polarized light, the proposed waveguides act as a source of cross-polarized photon pairs entangled both in polarization and in time-energy, i.e., entangled in more than one degree of freedom, or hyperentangled [46]. Such quantum states have multiple uses in quantum information processing, such as an improved reliability of quantum interference experiments [47] as well as superdense coding and cryptography [48,49]. On the other hand, when pumped by TM-polarized light, the proposed waveguides produce co-polarized photon pairs, which retain only time-energy entanglement. So, by varying the polarization of the pump light, one can control the degree of hyperentanglement in the generated photon pairs [26], which was found to be helpful for Bell state analysis [50].

3.2. Simultaneous phase matching of three types

We have seen that phase matching of two types can be used to generate both cross-polarized and co-polarized photon pairs, and switch between them easily. Still, the polarization of co-polarized pairs is predetermined: for the type II+I PM, they come from the type-I process and are always TE-polarized; for the type II+0 PM,

they come from the type-0 process and are always TM-polarized. It would be desirable to eliminate this certainty so that co-polarized photon pairs could be either TE+TE or TM+TM. This can be achieved by aligning all three PM types together at the same frequency ω_0 , i.e.,

$$n_{\text{eff}}^{\text{TE}}(2\omega_0) = n_{\text{eff}}^{\text{TM}}(2\omega_0) = n_{\text{eff}}^{\text{TE}}(\omega_0) = n_{\text{eff}}^{\text{TM}}(\omega_0). \quad (42)$$

Such alignment can be achieved by reducing Δn_{eff} to zero for both TIR-guided and Bragg-guided modes. This is only possible in a 2D geometry where Δn can be controlled by varying the ridge width W , as seen from Eqs. (38) and (39). From these equations, we note that the modes at ω are more strongly affected by changing the ridge width than modes at 2ω . Hence the route to achieve combined type I+II+0 PM in a BRW consists in lowering W to achieve $\Delta n_{\text{eff}}(\omega) = 0$ [see Fig. 9(a)] and maintaining PM in the desired wavelength range by simultaneously changing t_c . The claddings should be kept quarter-wave, which is achieved by adjusting $t_{h,l}$ to satisfy Eq. (32). Finally, the QW condition (32) needs to be slightly distorted to counteract a departure from $\Delta n_{\text{eff}}(2\omega) = 0$, which is once again done through a minor correction to t_c . The resulting structure, based on $x_c = 0.62$, $x_h = 0.2$, and $x_l = 0.8$ as in Fig. 7, has $t_c = 363.3$ nm, $t_h = 107$ nm, and $t_l = 262$ nm and shows the same n_{eff} for $W = 1.38 \mu\text{m}$ [see Fig. 9(b,c)]. The effective-index analytical results are seen to have a good agreement with 2D numerical simulations.

Having all three PM types at the same wavelength enables the proposed waveguide to generate entangled photon pairs with all possible polarization combinations (TE+TE from type I, TE+TM from type II, and TM+TM from type 0). Switching between cross-polarized pairs (TE+TM) and co-polarized pairs (TE+TE or TM+TM), similar to a conventional bulk two-crystal type-I SPDC source) can be achieved in the continuous-wave regime by simply rotating the polarization of the pump beam. In particular, this can enable on-chip generation of multiple optical Bell states, as will be discussed in the following section. In addition, combining all possible PM types at one wavelength can increase the brightness of a continuous-wave frequency upconversion device and make it polarization insensitive.

4. Entangled photon generation

One of the most promising features of SPDC in BRWs is to provide an on-chip source of entangled photons that can be integrated with other optical components such as a diode laser pump and quantum interference circuitry. As demonstrated in the previous section, the existence of waves with independent guiding mechanisms within the same BRW can be used to tailor SPDC parameters (such as wavelength, bandwidth, and PM type) via appropriate BRW-based structure design. However, the implications of this versatility on the nonclassical properties of generated photon pairs remain to be analyzed.

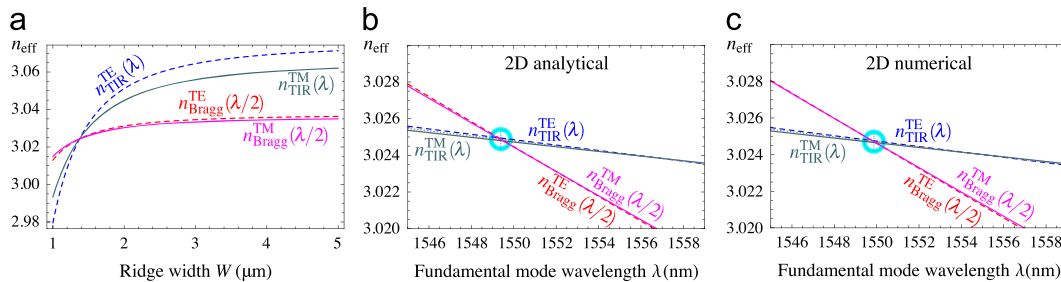


Fig. 9. (a) Dependence of mode effective indices on the ridge width W for a BRW with simultaneous three-type PM ($x_c = 0.62$, $t_c = 363.3$ nm; $x_h = 0.2$, $t_h = 107$ nm; $x_l = 0.8$, $t_l = 262$ nm) obtained analytically by the effective index method for $\lambda = 1550$ nm, along with the dispersion relations obtained (b) analytically and (c) numerically for the structure with $W = 1.38 \mu\text{m}$.

In what follows, we will combine the design principles outlined above with the previously developed quantum Hamiltonian treatment of SPDC in photonic waveguides [28,29] to determine the entanglement properties of photon pairs produced in BRWs and to design structures capable of generating interesting nonclassical states of light.

4.1. Cross-polarized photon pairs with maximal polarization entanglement

For many applications of photons in quantum information processing, it is desirable to have entanglement in only one degree of freedom, usually polarization. Generating such entangled photons on a chip turns out to be difficult because of form birefringence (see, e.g., Helmy et al. [51]). The birefringence causes group velocity mismatch (GVM) between differently polarized downconverted photons, so some information about a photon's polarization can be inferred from its spectral properties [52]. This limits the usefulness of polarization entanglement in quantum optical experiments [52–54].

To overcome this drawback, spectral filtering or off-chip post-compensation schemes are typically used [55]. Although such compensation can be implemented on-chip by a clever choice of polarization-transforming integrated optics (as recently demonstrated in a silicon-based SFWM source [6]), it would be highly desirable to find a universal method of eliminating form birefringence directly as the photon pairs are generated. Our primary objective is to use the presented analytical formalism to achieve $\Delta v_g = v_g^{\text{TM}} - v_g^{\text{TE}} = 0$ for the downconverted modes in a BRW.

We begin by considering a slab waveguide ($n_h = n_l = n_o$, i.e., no modulation in the cladding) and use Eq. (28) in the form of a generalized dependence $\Delta v_g = F(\omega, n_{\text{eff}})$. The effective index n_{eff} can be determined either numerically or from Eq. (16); Fig. 10(a) shows that both methods demonstrate decent qualitative agreement, so Eq. (16) can be used as a fast prediction tool for determining how Δv_g depends on the waveguide parameters. Thus, it can be seen that single-mode waveguides with small t_c do not satisfy $\Delta v_g = 0$ since $F(\omega, n_{\text{eff}}) > 0$. However, increasing the core thickness both increases $n_{\text{eff}}^{\text{TE}}$ and makes $F(\omega, n_{\text{eff}})$ cross zero. Hence a slab waveguide for TIR-guided modes with $v_g^{\text{TM}} = v_g^{\text{TE}}$ at a given ω can be designed simply by choosing the appropriate t_c .

In a BRW with modulated cladding, the expressions for r_{co} in Eq. (10) will be replaced by R_∞ from Eq. (31), and the expressions for δ_r in Eqs. (17) and (18) will be replaced by $\arg R_\infty$. So Δv_g is expected to depend on the modulation depth $n_h - n_l$. Still, it can be evaluated either semianalytically or numerically by using transfer matrix methods. Indeed, as seen in Fig. 10(b), the effect of the cladding modulation does not alter the dependence $\Delta v_g(t_c)$ qualitatively, and the quantitative modification is rather straightforward, so the appropriate t_c for zero GVM in the TIR-guided modes can still be selected.

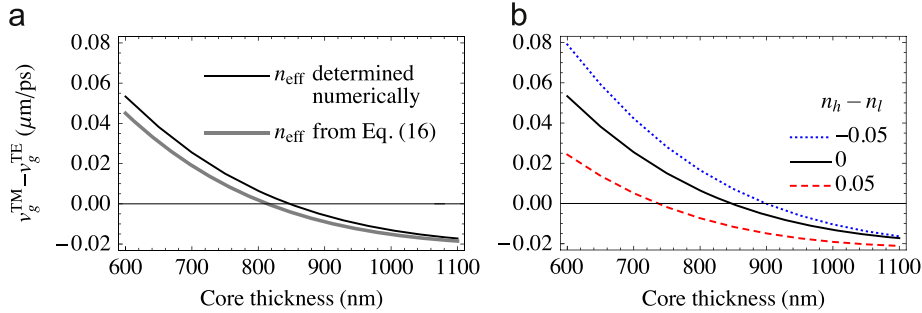


Fig. 10. (a) Comparison of the GVM $\Delta v_g = F(\omega, n_{\text{eff}})$ obtained from Eq. (28) with n_{eff} determined numerically vs. given by Eq. (16) for varying core thickness t_c . The structure is a slab $\text{Al}_x\text{Ga}_{1-x}\text{As}$ waveguide with $x_c = 0.4$ and $x_0 = 0.65$ ($n_c = 3.17$, $n_0 = 3.05$ at 1550 nm) and (b) the dependence $\Delta v_g(t_c)$ for different index modulation depth ($n_h - n_l$) in the Bragg cladding.

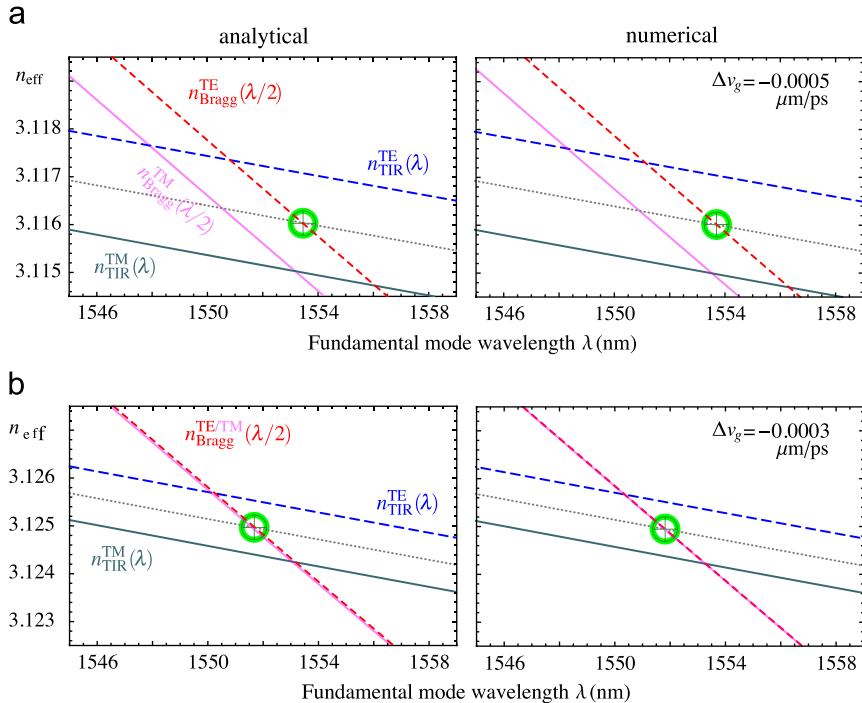


Fig. 11. Mode dispersion diagrams showing type-II PM in $\text{Al}_x\text{Ga}_{1-x}\text{As}$ BRWs ($x_c = 0.4$, $x_h = 0.6$, $x_l = 0.7$) with $\Delta v_g = 0$: (a) 1D slab with $t_c = 755$ nm, $t_h = 209$ nm, $t_l = 279$ nm; (b) 2D ridge with $t_c = 1014$ nm, $t_h = 232$ nm, $t_l = 341$ nm, and $W = 4.4 \mu\text{m}$, obtained analytically (left) and by a vectorial commercial mode solver [39] (right).

The next step is to phase match these modes with a Bragg-guided pump mode with the frequency $\omega_p = 2\omega$. For type-II PM, where a photon from the TE-polarized Bragg-guided mode will produce a pair of cross-polarized photons going into TE- and TM-polarized TIR-guided modes, we aim at $n_{\text{eff}}^{\text{TE}}(\omega) + n_{\text{eff}}^{\text{TM}}(\omega) = 2n_{\text{eff}}^{\text{TE}}(\omega_p)$. To maximize the reflectivity of the Bragg claddings, the cladding layer thicknesses should satisfy the QW condition (32) in the form [15]

$$t_h \sqrt{n_h^2 - n_{\text{eff}}^2(\omega_p)} = t_l \sqrt{n_l^2 - n_{\text{eff}}^2(\omega_p)} = (\lambda_p/2)/4 \equiv \Lambda, \quad (43)$$

and the pump mode should operate at the midgap point, i.e.,

$$h_c t_c = t_c \sqrt{n_c^2 - n_{\text{eff}}^2(\omega_p)} = m\Lambda, \quad m = 1, 2, 3, \dots. \quad (44)$$

Since $\Delta v_g = 0$ is fulfilled at relatively large values of $t_c \approx 700$ –900 nm, the fundamental Bragg mode for which $m=1$ cannot be phase matched at the desired n_{eff} [see, e.g., Fig. 5(c)]. Instead, we use the higher-order Bragg mode with $m=3$, which can be phase matched and whose spatial overlap with the fundamental downconverted modes is much better than for modes with even m .

The resulting example 1D design, based on $x_c = 0.4$, $x_h = 0.6$, $x_l = 0.7$ to keep the modulation depth in the cladding small, has

$t_c = 755$ nm, $t_h = 209$ nm, $t_l = 279$ nm. Fig. 11(a) shows a good agreement between analytically and numerically obtained dispersion relations. The numerical GVM for the downconverted modes equals $-5 \times 10^{-4} \mu\text{m}/\text{ps}$.

For the 2D ridge design, decreasing the ridge width W decreases Δn_{eff} (see Fig. 6) but increases Δv_g . Hence an additional increase in t_c is needed to compensate for it; t_h and t_l also have to be slightly increased to maintain PM at the desired wavelength due to the dependence of n_{eff} on W . The resulting 2D design for $W = 4.4 \mu\text{m}$ has $t_c = 1014$ nm, $t_h = 232$ nm, $t_l = 341$ nm. The corresponding dispersion diagrams are shown in Fig. 11(b), again demonstrating a good agreement between analytical and numerical results and showing GVM of $-3 \times 10^{-4} \mu\text{m}/\text{ps}$.

We can now employ the previously developed Hamiltonian treatment of $\chi^{(2)}$ -nonlinear processes in waveguide structures [28,29] to express the quantum state of a photon pair generated by SPDC as $|\psi^{\text{gen}}\rangle \approx (1 + \nu C_{\text{II}}^\dagger)|\text{vac}\rangle$ where C_{II}^\dagger is the biphoton creation operator

$$C_{\text{II}}^\dagger = \frac{1}{\sqrt{2}} \sum_{\alpha, \beta} \int_0^\infty d\omega_1 d\omega_2 \phi_{\alpha\beta}(\omega_1, \omega_2) a_{\alpha\omega_1}^\dagger a_{\beta\omega_2}^\dagger, \quad (45)$$

and $a_{\alpha\omega}$ are boson mode operators for the downconverted photons with frequency ω and polarization σ (TE or TM, or, respectively, H and

V), obeying the commutation relations $[a_{\sigma\omega}, a_{\sigma'\omega'}^\dagger] = \delta_{\sigma\sigma'} \delta(\omega - \omega')$. For details on calculating the rate of entangled photon generation in these structures, the reader is referred to our earlier works [14,54]. The function $\phi_{\alpha\beta}(\omega_1, \omega_2)$, called the biphoton wave function (BWF), characterizes the spectral properties of the generated photon pairs. It is symmetric with respect to the exchange of photons,

$$\phi_{\alpha\beta}(\omega_1, \omega_2) = \phi_{\beta\alpha}(\omega_2, \omega_1), \quad (46)$$

is normalized according to

$$\sum_{\alpha\beta} \int_0^\infty d\omega_1 d\omega_2 |\phi_{\alpha\beta}(\omega_1, \omega_2)|^2 = 1, \quad (47)$$

and has the form [14,28,29]

$$\phi_{\alpha\beta}(\omega_1, \omega_2) \propto \phi_p(\omega_1 + \omega_2) \text{sinc}(\Delta k_{\text{PM}}^{x\alpha\beta} L/2), \quad (48)$$

where $\phi_p(\omega)$ is the spectrum of the pump pulse, and

$$\Delta k_{\text{PM}}^{x\alpha\beta} = k_x(\omega_1 + \omega_2) - k_\alpha(\omega_1) - k_\beta(\omega_2) \quad (49)$$

is defined by the PM conditions. The wave vectors $k_\sigma(\omega)$ are determined from the waveguide dispersion relations (e.g., Fig. 11). Around the PM frequency ω_0 they are taken as

$$k_\sigma = k_{\sigma 0} + (\omega - \omega_0)/v_g^\sigma + (\omega - \omega_0)^2 \beta_2^\sigma/2, \quad (50)$$

where v_g^σ is the group velocity and where β_2^σ is the group velocity dispersion (GVD) parameter [56].

Assuming negligible GVD parameters, from Eqs. (48) and (50) it can be shown that zero GVM in the downconverted modes ($v_g^{\text{TM}} = v_g^{\text{TE}}$) results in additional symmetries in the BWF:

$$\begin{aligned} \phi_{\alpha\beta}(\omega_1, \omega_2) &= \phi_{\alpha\beta}(\omega_2, \omega_1) \\ \text{or } \phi_{\alpha\beta}(\omega_1, \omega_2) &= \phi_{\beta\alpha}(\omega_1, \omega_2). \end{aligned} \quad (51)$$

The degree to which these symmetries are truly satisfied, regardless of the size of the GVD parameters or GVM, can be quantified by the parameters [53]

$$G_{\alpha\beta} = 2 \int d\omega_1 d\omega_2 \phi_{\alpha\beta}(\omega_1, \omega_2) \phi_{\beta\alpha}^*(\omega_1, \omega_2). \quad (52)$$

We note that it is non-trivial to define a fidelity between our multi-frequency (multimode) states $C_{||}^\dagger |vac\rangle$ [recall Eq. (45)] and the “ideal single-mode” (single-frequency) polarization-encoded Bell states of the literature $|\Psi^\pm\rangle = [|HV\rangle \pm |VH\rangle]/\sqrt{2}$ and $|\Phi^\pm\rangle = [|HH\rangle \pm |VV\rangle]/\sqrt{2}$, as our states contain frequency correlations whereas the “ideal” states ignore the frequency degree of freedom.

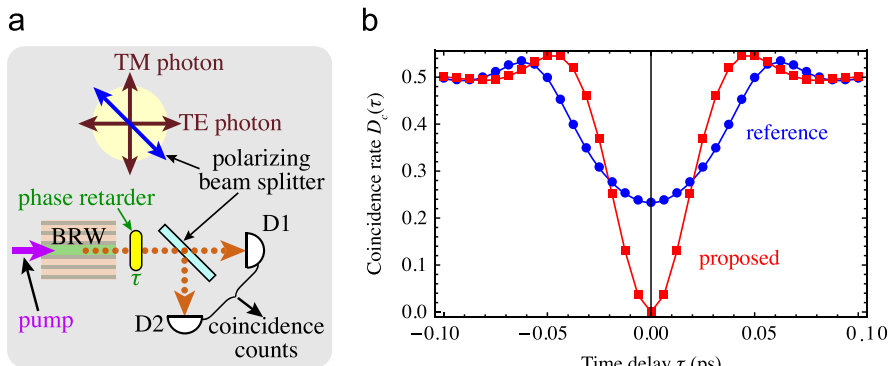


Fig. 12. (a) The schematic of a HOM-type experiment to verify the degree of polarization entanglement [52,53]; (b) the calculated coincidence rate $D_c(\tau)$ as per Eq. (55) for the proposed structure with mode dispersion shown in Fig. 11(b) compared to the reference structure from Fig. 7(c). Note that the zero in the time scale is relative and depends on the walk-off effects arising from polarization sensitive elements of the experimental set-up (including the waveguide itself if $\Delta v_g \neq 0$); this walk-off can be easily compensated.

Nevertheless, when $G_{HV} = G_{HV}^* = 1$ then Eq. (51) holds and the state corresponding to cross-polarized photon pairs

$$\begin{aligned} C_{HV,VH}^\dagger |vac\rangle &= \frac{1}{\sqrt{2}} \int d\omega_1 d\omega_2 [\phi_{HV}(\omega_1, \omega_2) a_{H\omega_1}^\dagger a_{V\omega_2}^\dagger \\ &\quad + \phi_{VH}(\omega_1, \omega_2) a_{V\omega_1}^\dagger a_{H\omega_2}^\dagger] |vac\rangle, \end{aligned} \quad (53)$$

can be written as

$$|\psi^{\text{sym}}\rangle = \int d\omega_1 d\omega_2 \phi_{HV}(\omega_1, \omega_2) \frac{a_{H\omega_1}^\dagger a_{V\omega_2}^\dagger + a_{V\omega_1}^\dagger a_{H\omega_2}^\dagger}{\sqrt{2}} |vac\rangle. \quad (54)$$

The states $|\psi^{\text{sym}}\rangle$ and $|\Psi^+\rangle$ behave identically in a class of experiments that includes fourth-order interference experiments [52,53], as well as the polarization-correlation and Bell state analyzer experiments of [57]. Furthermore, note that the fidelity between the states $C_{HV,VH}^\dagger |vac\rangle$ and $|\psi^{\text{sym}}\rangle$ [Eqs. (53) and (54)] is simply $F = |1 + G_{HV}|/2$. Hence, we refer to photon pairs for which $G_{HV} = G_{HV}^* = 1$ as maximally polarization entangled [54].

One such experiment is the Hong-Ou-Mandel-type experiment shown in Fig. 12(a) [52]. There the polarizing beam splitter oriented diagonally between TE and TM polarizations acts as a 50:50 beam splitter for both photons, so if they are entangled, the detectors should register no coincidence counts. Varying the time delay τ between the two polarizations, created by placing a birefringent phase retarder before the beam splitter, one should see a dip in the dependence of the coincidence rate $D_c(\tau)$. For a more general type-II state for which Eq. (51) does not hold, $D_c(\tau)$ assumes the form [52]

$$D_c(\tau) = \int d\omega_1 d\omega_2 [|\phi_{HV}(\omega_1, \omega_2)|^2 - \phi_{HV}(\omega_1, \omega_2) \phi_{VH}^*(\omega_1, \omega_2) e^{i(\omega_1 - \omega_2)\tau}]. \quad (55)$$

It is found numerically that the design in Fig. 11(b) has $G_{HV} = 1 - 1.6 \times 10^{-6}$ as opposed to $G_{HV} = 0.537$ for the reference structure in Fig. 7 [54], and clearly seen in Fig. 12(b) that the proposed structure offers a much greater visibility of the HOM dip, $V = G_{HV}/(2 - G_{HV})$, than the reference structure ($1 - 3 \times 10^{-6}$ versus 0.37). Thus it is confirmed that the proposed analytical methods can optimize the performance of BRW-based polarization entangled photon sources. Note that dispersive elements of the experimental set-up (including the waveguide itself) can introduce frequency-dependent walk-off between TE- and TM-polarized downconverted photons as they travel from where they are generated (taken to be the center of the waveguide in the scattering theory formalism of Yang et al. [29]). For sufficiently broadband SPDC, this can cause τ in Eq. (55) to become frequency-dependent [$\tau \rightarrow \tau(\omega_1, \omega_2)$] and alter the shape of the HOM dip, possibly decreasing its visibility [58]. We are neglecting this effect

here because it is fully classical, and in principle could be compensated by using an opposite-signed dispersive element [59].

4.2. Co-polarized and cross-polarized entangled photon pairs with a single source: towards on-chip generation of Bell states

Finally, we combine the reasoning of Sections 3.2 and 4.1 to design structures with even more possibilities for on-chip quantum optics. One such possibility is the generation of entangled photons with all possible polarization combinations (TE+TM, TE+TE, and TM+TM) at the same pump wavelength, while keeping the degree of polarization entanglement at the maximum. Such a photon pair source would be able to generate high-quality co-polarized and cross-polarized entangled photon pairs, and would potentially facilitate on-chip production of optical Bell states [18,19].

For this to be achieved, we would need a structure with both group and phase velocities of the downconverted modes rendered equal, e.g., $v_g^{\text{TM}} = v_g^{\text{TE}}$ and $n_{\text{eff}}^{\text{TE}} = n_{\text{eff}}^{\text{TM}}$. Additionally, the Bragg claddings should remain QW so that simultaneous PM of all three types is present.

The strategy to design the desired structure is to simultaneously control Δn_{eff} (by varying the ridge width W) and Δv_g (by varying the core thickness t_c and taking into account the effect of W) in an iterative manner. The cladding parameters are chosen so as to satisfy the QW condition (32) for the target value of n_{eff} , and the points in the (t_c, W) space where $\Delta v_g = 0$ and $\Delta n_{\text{eff}} = 0$ are brought together by a slight (on the order of 0.005) adjustment to that target value.

The design target for the Al concentrations in the layers $x_c = 0.4$, $x_h = 0.2$, $x_l = 0.8$ and thicknesses $t_c = 1900$ nm, $t_h = 107$ nm, $t_l = 264$ nm is at $W = 1.52 \mu\text{m}$ [Fig. 13(a)]. Both analytical and numerical results demonstrate simultaneous PM of all three types. Minute discrepancies between Fig. 13(b,c) are associated with the finite number of periods ($N=10$) in the numerical simulations, whereas the analytical model assumes that the number of periods is infinite.

The numerically determined GVM in this design is $\Delta v_g \approx 0.1 \mu\text{m}/\text{ps}$, which is worse than in the previous section but can be further reduced by iterative parameter tuning. Still, for the TE-polarized pump (type-II PM, cross-polarized photon pairs) Eq. (52) gives $G_{HV} = 0.923$. This value is much closer to unity than the reference design in Fig. 7. It also surpasses the 3-type PM structure in Fig. 9, which is more similar in geometrical composition and has $G_{HV} = 0.2$. Additionally, we have calculated the shape of the dip for the HOM-type experiment of Fig. 12(a). Even though $D_c(\tau=0) \approx 0.03 > 0$, the dip has visibility of 0.857, which is much more pronounced than for the other structures [Fig. 14(a)].

The need to use a 3rd-order Bragg mode as a pump, which was required to achieve zero GVM, decreases the pair production efficiency, which amounts to $\eta_{II} = 5.4 \times 10^{-9}$ pairs per pump photon for the type-II process and one order of magnitude weaker

for the type-I and type-0 processes ($\eta_I = 5.3 \times 10^{-10}$ and $\eta_0 = 4.6 \times 10^{-10}$ pairs per pump photon). We see that the proposed structure has $\eta_0 \approx \eta_I$, unlike most BRWs where $\eta_0 \ll \eta_I$ because the type-0 process relies on the weak z-components of the modes. Along the same lines as discussed in earlier [13], comparable efficiencies of type-I and type-0 processes make it possible to use the structure to produce co-polarized entangled photon pairs using a TM-polarized pump, where the generated photon pair (having either TE+TE or TM+TM polarization) is such that its polarization state is unknown, but measuring the polarization of one photon unambiguously identifies the polarization of the other.

To demonstrate the improved performance for the co-polarized pairs, we imagine subjecting them to the same experiment as the cross-polarized photons [Fig. 12(a)]. In this case, the expression for the coincidence rate is different and depends on τ much more strongly:

$$D_c(\tau) = \frac{1}{2} \int d\omega_1 d\omega_2 (|\phi_{HH}(\omega_1, \omega_2)|^2 + |\phi_{VV}(\omega_1, \omega_2)|^2 - |\phi_{HH}(\omega_1, \omega_2)\phi_{VV}^*(\omega_1, \omega_2)e^{i(\omega_1+\omega_2)\tau} + \text{c.c.}|)^2 \quad (56)$$

Note that, unlike for cross-polarized photons, this rate does not necessarily drop to zero if the two processes associated with $\phi_{HH}(\omega_1, \omega_2)$ and $\phi_{VV}(\omega_1, \omega_2)$ have identical spectra [cf. Eq. (52)]. Here it is also required that the two processes have identical efficiencies, i.e., $\int d\omega_1 d\omega_2 |\phi_{HH}(\omega_1, \omega_2)|^2 = \int d\omega_1 d\omega_2 |\phi_{VV}(\omega_1, \omega_2)|^2$ [or analogously, $G_{HH} = G_{VV}$ from Eq. (52)], a condition satisfied automatically for our cross-polarized photon pairs.

In contrast to the cross-polarized case where the phase retarder delays one photon in a pair, thus destroying the quantum interference so that $D_c \rightarrow 0.5$ for large τ , in the co-polarized case delaying TE-polarized photon pairs with respect to the TM ones just introduces a phase shift between the corresponding HH and VV portions in the BWF, changing the quantum interference pattern and resulting in fringes. The visibility of these fringes can still characterize the degree of polarization entanglement between the photons. In the ideal case of $\eta_0 = \eta_I$ and $\phi_{HH}(\omega_1, \omega_2) = \phi_{VV}(\omega_1, \omega_2)$, $D_c(\tau)$ reaches its minimum of zero at $\tau = 0$ and maximum of unity for a certain τ ; this corresponds to the maximal polarization entanglement. Otherwise, the visibility of fringes is reduced, and in the other limiting case (either $\eta_0 \ll \eta_I$ or no spectral overlap between ϕ_{HH} and ϕ_{VV}) the fringes completely vanish, giving $D_c = 1/2$.

The results, shown in Fig. 14(b), confirm that the optimized design shows a much greater visibility of interference fringes than the earlier design (0.91 vs. under 0.002). Hence the proposed structure has a potential of being used as a source of multiple optical Bell states with very simple switching involving just a change of the incoming pump polarization. This potential, along with further nonclassical properties of generated photon pairs, will be analyzed in more detail in a future study.

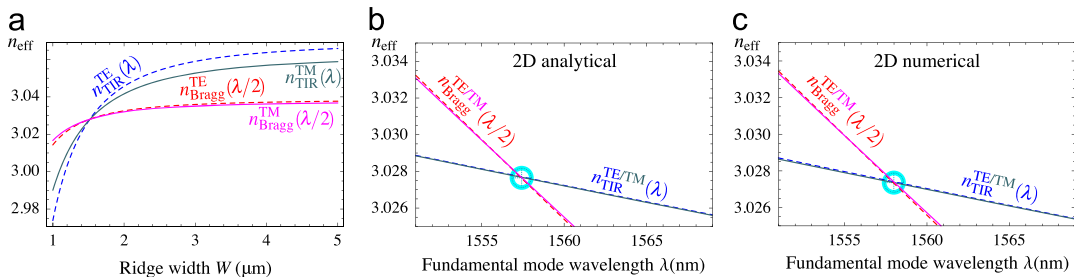


Fig. 13. (a) Dependence of mode effective indices on the ridge width W for a BRW with simultaneous three-type PM and zero GVM in the fundamental modes ($x_c = 0.4$, $t_c = 1900$ nm; $x_h = 0.2$, $t_h = 107$ nm; $x_l = 0.8$, $t_l = 264$ nm) obtained analytically by the effective index method for $\lambda = 1550$ nm, along with the dispersion relations obtained (b) analytically and (c) numerically for the structure with $W = 1.52 \mu\text{m}$.

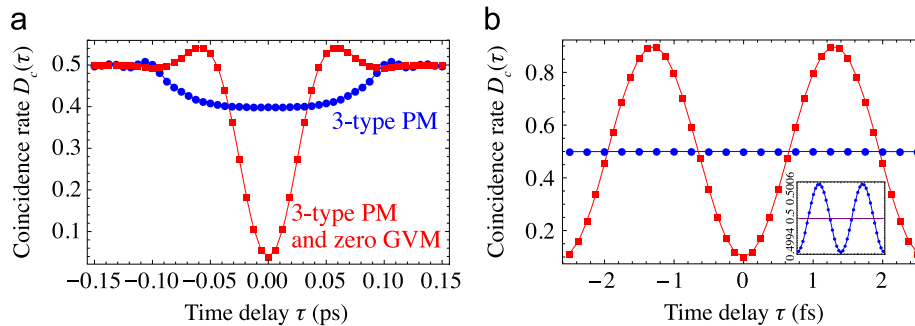


Fig. 14. The calculated coincidence rate $D_c(\tau)$ for the proposed zero-GVM structure (Fig. 13) compared to the non-optimized structure featuring simultaneous 3-type PM (Fig. 9): (a) HOM-like dip for cross-polarized photons, as per Eq. (55); (b) quantum beats for co-polarized photons, as per Eq. (56). The inset shows an enlarged view of the non-optimized curve, revealing that there are quantum beats but with a very small visibility (< 0.002).

5. Conclusions

To summarize, we have developed an analytical description of multilayer slab and ridge waveguides using a combination of Fresnel and recurrent Airy formulas with the use of the effective index method. We have shown that it is often possible to construct approximate but simple and straightforward analytical expressions describing the effective indices and group velocities of guided modes in arbitrary 1D Bragg reflection waveguides (BRWs), and have defined the range of applicability for these expressions in terms of the waveguide parameters. The derived expressions simplify the calculations involving multilayer waveguides as compared with the more traditional transfer matrix methods or direct stitching of Maxwell's equation solutions at layer interfaces [23,24], especially when inverse problems are involved. The presented examples demonstrate a good agreement between analytical and numerical results.

Specifically, the approach has been employed in the design of BRWs with predetermined properties. First, we have designed BRWs where two or three distinct PM types are present simultaneously at the same wavelength. This can enrich the degree of polarization-driven control over nonlinear frequency conversion processes and produce photon pairs entangled in a controllable number of degrees of freedom [26]. Second, we have designed BRWs for SPDC processes where the downconverted modes have similar phase and/or group velocity. This can optimize the entanglement characteristics of generated photons, maximizing the degree of polarization entanglement in them [54]. Such structures can promote the use of BRWs as on-chip sources of entangled photons and Bell states, furthering the goal of bringing quantum optical experiments from an optical table to an optical chip. The latter becomes especially relevant because the proposed designs are based on an already mature AlGaAs fabrication platform where integration of an SPDC photon pair source with a diode laser pump has already been a success [60], making the results obtained in the present study directly suitable for an experimental realization. As a first step, a very recent paper [12] shows an experimental demonstration of type-I SPDC in a BRW. Complementary to the recent success in implementing an SFWM-based entangled photon source on a silicon chip [6], SPDC-based entangled photon sources in AlGaAs would enrich the variety of available components for on-chip quantum optical experiments and quantum information systems.

We note that while a BRW is an elegant example of a waveguide with complex multilayer structure, it is certainly not the only example. Closely related to BRWs are multilayer structures supporting Bloch surface waves, which are used in metal-free surface enhanced Raman scattering [61] and as a mechanism to form guided exciton polaritons [62]. Recently proposed hybrid photonic/plasmonic waveguides, which combine low absorption

losses with nanoscale light confinement, are essentially multilayer waveguides comprised of high-index, low-index, and metal layers [63]. Finally, deeply subwavelength metal-dielectric multilayers, commonly regarded as hyperbolic metamaterials [64], can be shown to support a multitude of both guided and bulk propagating waves arising from coupled surface plasmon excitations [65], and can also be described within the approach presented here.

Acknowledgments

This work was supported by the Natural Sciences and Engineering Research Council of Canada (NSERC).

References

- [1] K. Vahala, Optical Microcavities, World Scientific, Singapore, 2004.
- [2] G. Roelkens, L. Liu, D. Liang, R. Jones, A. Fang, B. Koch, J. Bowers, Lasers & Photonics Reviews 4 (2010) 751.
- [3] C. Junge, S. Nickel, D. O'Shea, A. Rauschenbeutel, Optics Letters 36 (2011) 3488.
- [4] L. Liu, G. Roelkens, J. Van Campenhout, J. Brouckaert, D. Van Thourhout, R. Baet, Journal of Nanoscience and Nanotechnology 10 (2010) 1461.
- [5] J.L. O'Brien, A. Furusawa, J. Vučković, Nature Photonics 3 (2009) 687.
- [6] N. Matsuda, H. Le Jeannic, H. Fukuda, T. Tsuchizawa, W.J. Munro, K. Shimizu, K. Yamada, Y. Takura, H. Takesue, Science Reports 2 (2012) 817.
- [7] A.S. Helmy, Optics Express 14 (2006) 1243.
- [8] J. Han, P. Abolghasem, B.J. Bijlani, A.S. Helmy, Optics Letters 34 (2009) 3656.
- [9] J. Han, P. Abolghasem, D. Kang, B.J. Bijlani, A.S. Helmy, Optics Letters 35 (2010) 2334.
- [10] P. Abolghasem, J. Han, B.J. Bijlani, A. Arjmand, A.S. Helmy, IEEE Photonics Technology Letters 21 (2009) 1462.
- [11] J. Svozilík, M. Hendrych, A.S. Helmy, J.P. Torres, Optics Express 14 (2011) 3115.
- [12] R. Horn, P. Abolghasem, B.J. Bijlani, D. Kang, A.S. Helmy, G. Weihs, Physical Review Letters 108 (2012) 153605.
- [13] D. Kang, A.S. Helmy, Optics Letters 37 (2012) 1481.
- [14] S.V. Zhukovsky, L.G. Helt, P. Abolghasem, D. Kang, J.E. Sipe, A.S. Helmy, Journal of the Optical Society of America B 29 (2012) 2516.
- [15] B.R. West, A.S. Helmy, IEEE Journal of Selected Topics in Quantum Electronics 12 (2006) 431.
- [16] P. Abolghasem, J.B. Han, B.J. Bijlani, A.S. Helmy, Optics Express 18 (2010) 12861.
- [17] S.L. Braunstein, A. Mann, M. Revzen, Physical Review Letters 68 (1992) 3259.
- [18] Y. Shih, IEEE Journal of Selected Topics in Quantum Electronics 9 (2003) 1455.
- [19] P.G. Kwiat, K. Mattle, H. Weinfurter, A. Zeilinger, A.V. Sergienko, Y. Shih, Physical Review Letters 75 (1998) 4337.
- [20] M.G. Thompson, A. Politi, J.C.F. Matthews, J.L. O'Brien, IET Circuits, Devices & Systems 5 (2011) 94.
- [21] L. Sansoni, F. Sciarrino, G. Vallone, P. Mataloni, A. Crespi, R. Ramponi, R. Osellame, Physical Review Letters 105 (2010) 200503.
- [22] T.D. Ladd, F. Jelezko, R. Laflamme, Y. Nakamura, C. Monroe, J.L. O'Brien, Nature 464 (2010) 45.
- [23] B.R. West, A.S. Helmy, Journal of the Optical Society of America B 23 (2006) 1207.
- [24] B.R. West, A.S. Helmy, Optics Express 14 (2006) 4073.
- [25] P. Abolghasem, A.S. Helmy, IEEE Journal of Quantum Electronics 45 (2009) 646.
- [26] S.V. Zhukovsky, D. Kang, P. Abolghasem, L.G. Helt, J.E. Sipe, A.S. Helmy, Optics Letters 36 (2011) 3548.
- [27] S. Chakraborty, M.C. Parker, R.J. Mears, Photonics and Nanostructures Fundamentals and Applications 3 (2005) 139.
- [28] L.G. Helt, E.Y. Zhu, M. Liscidini, Li Qian, J.E. Sipe, Optics Letters 34 (2009) 2138.

- [29] Z. Yang, M. Liscidini, J.E. Sipe, *Physical Review A* 77 (2008) 033808.
- [30] J.J. Saarinen, J.E. Sipe, *Journal of Modern Optics* 55 (2008) 13.
- [31] H. Kogelnik, *Integrated Optics: Topics on Applied Physics*, vol. 7, Springer, Berlin, 1972, pp. 13–81.
- [32] A. Yariv, P. Yeh, *Optical Waves in Crystals*, Wiley, New York, 1983.
- [33] J.E. Sipe, *Solid State Communications* 39 (1981) 493.
- [34] S.A. Shakir, A.F. Turner, *Applied Physics A* 29 (1982) 151.
- [35] M. Liscidini, J.E. Sipe, *Journal of the Optical Society of America B* 26 (2009) 279.
- [36] A. Yariv, P. Yeh, *Photonics: Optical Electronics in Modern Communications*, Oxford University Press, USA, 2007.
- [37] S. Gehrsitz, F.K. Reinhart, C. Gourgon, N. Herres, A. Vonlanthen, H. Sigg, *Journal of Applied Physics* 87 (2000) 7285.
- [38] S.V. Zhukovsky, *Physical Review A* 81 (2010) 053808.
- [39] MODE SOLUTIONS, version 4.0, Lumerical Solutions, Inc. (www.lumerical.com).
- [40] K.S. Chang, W.P. Wong, *IEEE Journal of Quantum Electronics* 35 (1999) 1554.
- [41] W.P. Wong, K.S. Chang, *IEEE Journal of Quantum Electronics* 37 (2001) 1138.
- [42] A.M. Schöber, M. Charbonneau-Lefort, M.M. Fejer, *Journal of the Optical Society of America B* 22 (2005) 1699.
- [43] P. Abolghasem, J. Han, B.J. Bijlani, A.S. Helmy, *Optics Express* 18 (2010) 12681.
- [44] V. Pasiskevicius, S.J. Holmgren, S. Wang, F. Laurell, *Optics Letters* 27 (2002) 1628.
- [45] B.F. Johnston, P. Dekker, M.J. Withford, S.M. Saltiel, Yu.S. Kivshar, *Optics Express* 14 (2006) 11756.
- [46] P.G. Kwiat, *Journal of Modern Optics* 44 (1997) 2173.
- [47] D.V. Strekalov, T.B. Pittman, A.V. Sergienko, Y.H. Shih, P.G. Kwiat, *Physical Review A* 54 (1996) R1.
- [48] J.T. Barreiro, N.K. Langford, N.A. Peters, P.G. Kwiat, *Physical Review Letters* 95 (2005) 260501.
- [49] A. Hayat, P. Ginzburg, D. Neiman, S. Rosenblum, M. Orenstein, *Optics Letters* 33 (2008) 1168.
- [50] P.G. Kwiat, H. Weinfurter, *Physical Review A* 58 (1998) R2623.
- [51] A.S. Helmy, P. Abolghasem, J.S. Aitchinson, B. Bijlani, J. Han, B.M. Holmes, D. C. Hutchings, U. Younis, S.J. Wagner, *Laser & Photonics Reviews* 5 (2011) 272.
- [52] W.P. Grice, I.A. Walmsley, *Physical Review A* 56 (1997) 1627.
- [53] T.S. Humble, W.P. Grice, *Physical Review A* 77 (2008) 022312.
- [54] S.V. Zhukovsky, L.G. Helt, D. Kang, P. Abolghasem, A.S. Helmy, J.E. Sipe, *Physical Review A* 85 (2012) 013838.
- [55] D. Branning, W.P. Grice, R. Erdmann, I.A. Walmsley, *Physical Review Letters* 83 (1999) 955.
- [56] G.P. Agrawal, *Nonlinear Fiber Optics*, 4th ed., Academic Press, Burlington, MA, 2007, p. 8.
- [57] A.B. U'Ren, K. Banaszek, I.A. Walmsley, *Quantum Information and Computation* 3 (2003) 480.
- [58] J. Peřina Jr., A.V. Sergienko, B.M. Jost, B.E.A. Saleh, M.C. Teich, *Physical Review A* 59 (1999) 2359.
- [59] M.H. Rubin, D.N. Klyshko, Y.H. Shih, A.V. Sergienko, *Physical Review* 50 (1994) 5122.
- [60] B. Bijlani, P. Abolghasem, A. Reijnders, A.S. Helmy, in: *CLEO: 2011 Postdeadline Papers*, Optical Society of America, Washington, DC, 2011, PDPA3.
- [61] A. Delfan, M. Liscidini, J.E. Sipe, *Journal of the Optical Society of America B* 29 (2012) 1863.
- [62] M. Liscidini, D. Gerace, D. Sanvitto, D. Bajoni, *Applied Physics Letters* 98 (2011) 121118.
- [63] M. Wu, Z. Han, V. Van, *Optics Express* 18 (2010) 11728.
- [64] C.L. Cortes, W. Newman, S. Molesky, Z. Jacob, *Journal of Optics* 14 (2012) 063001.
- [65] O. Kidwai, S.V. Zhukovsky, J.E. Sipe, *Physical Review A* 85 (2012) 053842.